J. Fluid Mech. (1988), *vol.* 193, *pp.* 285–302
Printed in Great Britain

Visualization of coating flows

By PETER M. SCHWEIZER
Ilford AG, Industriestrasse 15, CH-1701 Fribourg, Switzerland

(Received 6 December 1986 and in revised form 6 January 1988)

An experimental technique for visualizing small-scale film flows is presented. The method utilizes hydrogen bubbles, dye injection, and optical sectioning. Specific aspects of applying this technique to coating processes, distinguished by two free surfaces, liquid–liquid interfaces, static and dynamic wetting lines, and small characteristic dimensions, are discussed in detail. This experimental approach is essential in providing the necessary boundary conditions for modern computer-aided theoretical computations of wetting-related flow fields. The power of the visualization method is demonstrated by examples showing the flow pattern of two liquid films merging on an inclined plane and the flow field of a liquid film being transferred from an inclined plane onto a moving surface.

1. Introduction

A coating process is characterized by one fluid replacing another fluid on a surface; in most technical applications, liquid is replacing air on a moving, solid substrate.

In recent years, coating processes have attracted the interest of the scientific community for two reasons. New industries that utilize coating operations have evolved, such as semiconductor component or magnetic media manufacturing. In addition, productivity and uniformity requirements of coating operations in well-established industries, like silver halide photography, have increased.

There are two basic classes of coating processes that involve the formation and application of a coherent liquid film onto a moving substrate. They are called premetered and self-metered coating flows. Each class offers various coating modes. Their characteristic flow fields have recently been discussed in a review article by Ruschak (1985).

Premetered coating flows are the class of choice in the photographic industry because the coating thickness, which is the property of chief interest, is an independent parameter that can be easily controlled and varied within limits. The feature of simultaneous multilayer application makes *slide coating* the most attractive mode for this industry.

Premetered coating flows (the subject of this paper) are highly two-dimensional flow fields, characterized by two free surfaces, static and dynamic wetting lines, and very small characteristic dimensions, typically on the order of 100 μm. These complex features are the reason that most of the past theoretical analyses, in particular analytical approaches, have been relatively unsuccessful in explaining precise relationships between relevant parameters that govern such flows. It was only with the introduction of numerical methods to the discipline of fluid dynamics that the underlying physical principles of coating processes have been analysed more accurately, and the results thereof have been made available to a broader public.

A comprehensive overview of these efforts was published by Kistler & Scriven

(1983). In it, they depict calculations of base flows of various coating processes in the form of streamline plots, which are essentially flow-visualization experiments performed on the computer. While these results reveal details of these flow fields, such as flow separations or shapes and positions of free liquid surfaces (unseen heretofore), they suffer from the fact that the boundary conditions at the dynamic and static wetting lines are not known and must be assumed. These assumptions, if made improperly, affect the local solution of the flow field near the wetting lines. In fact, as will be shown herein, the results may turn out to be unrealistic.

This situation clearly points out the need for an experimental flow-visualization technique that is equally able to display free-surface profiles, as well as subtle details of the two-dimensional flow fields including wetting lines.

Previous experimental work on visualization methods for coating flows is sparse. Tallmadge, Weinberger & Faust (1979), Kobayashi, Saito & Scriven (1982), and Kraegel, Fruhner & Kretzschmar (1987) each show one or more photographs of the cross-sectional view of the slide coating process, concentrating on the free-surface profiles. None of the pictures present information about the inside of the flow field. Further, the authors hardly, if at all, discuss the respective effects of parameter variations. Other photographs of two-dimensional, coating-related flow fields include the interfacial region of a tape plunging into a tank filled with static fluid (Burley & Kennedy 1976), and the formation of a liquid curtain as it becomes detached from the tip of an inclined plane (Kistler 1983). The latter pictures were taken at an oblique angle; therefore, they do not represent a truly two-dimensional view.

In this paper, an experimental flow-visualization technique featuring the following characteristics is presented: (i) a detailed display of the inside of the two-dimensional flow field via streamlines; (ii) an indication of the true position and shape of free liquid surfaces, including dynamic and static wetting lines and apparent contact angles; and (iii) a simple and inexpensive implementation.

The visualization method that is able to meet the above requirements is a combination of hydrogen bubbles, dye injection, and optical sectioning techniques. It will be explained in detail in the next section.

The purpose of this work is to show, for the first time, accurate photographs of characteristic flow patterns of coating flows. Here, the slide coating mode has been chosen as an illustrative example, but the visualization technique is applicable to many other coating processes or thin-film flows. We hope that these pictures will stimulate theoretical research to obtain a better understanding of phenomena such as air entrainment, stability of coating flows, and product quality improvement through process optimization.

Last, but not least, these photographs present an artistic and aesthetic aspect of the otherwise rather technical and scientific coating processes.

2. Experimental set-up

The visualization of coating flows is made difficult by their small characteristic dimensions. Any successful experimental technique must, therefore, utilize an optical device for magnification. Even though only one of the two optical paths through the instrument is needed, a stereo zoom microscope is most suitable because its relatively large working distance allows sufficient penetration into the flow field past any possible edge effects, and the zoom mechanism can easily vary magnification. More importantly, this microscope has a very small depth of field. Consequently, only a thin slice of the flow field can be rendered sharp on the image

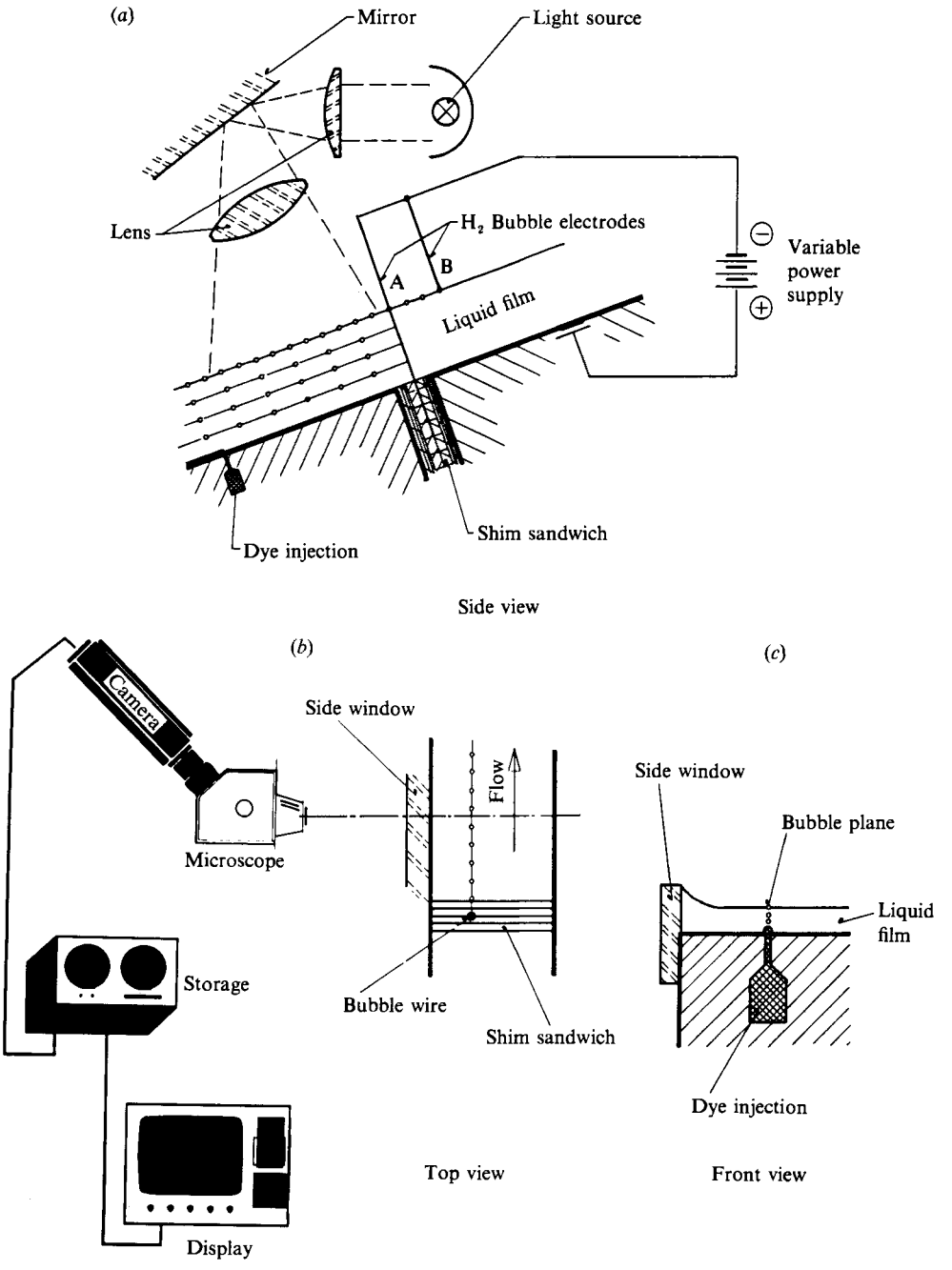

FIGURE 1. Experimental set-up.

plane of the device. Thus, if we succeed in generating a streamline pattern that coincides with the focal plane of the microscope, we can obtain sharp photographs, free of optical noise, revealing detailed information of the two-dimensional flow field.

As schematically shown by dotted lines in figure 1(*a*), the streamlines of a liquid film on an inclined plane are made visible by local and controlled injection of a tracer,

which subsequently is properly illuminated. In this case, the 'tracer particles' are hydrogen bubbles, created by the electrolysis of an aqueous solution. The electrolysis circuit is driven by a d.c. power supply. The positive electrode can be any metal part located anywhere in the flow field, but a convenient electrode is the inclined plane itself, if it is metallic. The hydrogen-bubble-producing negative electrode (position A in figure 1 *a*) is a thin wire that is clamped between two segments of the inclined plane and fastened a short distance above the film surface, such that it is stretched and oriented perpendicular to the inclined plane. Two thin plastic shims provide a sandwich-like electrical insulation between the positive and negative electrodes. Finally, the electrolysis circuit is closed by the liquid film itself, which must be sufficiently conductive.

The fundamental details of the hydrogen-bubble visualization technique will not be discussed here; instead, attention is focused on how it can be applied most efficiently to thin film and coating flows. Two good overviews of this technique were published by Clutter & Smith (1961) and Schraub *et al.* (1965).

As the liquid film flows past the wire electrode, hydrogen bubbles are swept off the wire and transported downstream where they describe the streamline pattern of the flow field. In figure 1 (*a*), this is indicated by parallel, dotted lines in the liquid film, detaching from the wire on its downstream side.

Each streamline originates at a randomly distributed nucleation point along the submerged portion of the wire. As the wire starts to be contaminated during operation, owing to corrosion and/or deposition of salts, the distribution of nucleation sites changes and their number may decrease, resulting in the loss of flow information. Although any metal serves well as wire material, platinum is preferred, because of its high corrosion resistance. Schraub *et al.* (1965) suggest that a contaminated wire should be cleaned by reversing the polarity on the wire for a couple of minutes. In addition, we found that gentle mechanical scrubbing of the wire, e.g. with a fine wooden rod, works well.

It is obvious that the electrode wire introduces a local disturbance to the flow field, not only in terms of the velocity profile in the wake of the wire, but also on the film surface where a pair of standing waves grow in an arrow-like manner in the downstream direction from the wire towards the edges of the film; see, for example, Schweizer & Scriven (1983). Since these standing waves grow away from the bubble plane, they will not be imaged by the microscope; whether or not their existence is of concern at all depends on the type of information to be extracted from the flow-visualization photos. If only qualitative results are of interest, the standing waves can be disregarded.

Clutter & Smith (1961) postulated that in order for the disturbance effect of the wire electrode to be negligible the Reynolds number based upon the wire diameter must be < 40.0. Replacing the characteristic velocity in the Reynolds number by the average velocity of a film on an inclined plane, one obtains the following condition for the diameter of the wire electrode, d_w:

$$d_w < 40\left(\frac{3\nu^4}{g\cos\beta Q^2}\right)^{\frac{1}{3}}. \tag{1}$$

Q is the volumetric flow rate per unit width, ν is the kinematic viscosity, g is the acceleration due to gravity, and β is the slide angle with respect to the vertical. Throughout our experiments, we used a platinum wire with a diameter of 127 μm, which satisfied (1) for a wide range of flow conditions.

The size of the hydrogen bubbles depends on the wire diameter. For water–glycerin solutions, used in all our experiments, we estimated from photographs that the bubble diameter was ≈ 2.5 to 7.5 times smaller than the wire diameter. We also observed that the bubble size decreases with both increasing fluid velocity and liquid viscosity. The bubble size is a critical parameter, because a streamline pattern can be reproduced accurately only if the ratio of buoyant force to drag force is $\ll 1.0$. If we compare the rise velocity u of a bubble in a quiescent tank as described by Stokes flow, with the average velocity U of a film on an inclined plane, this ratio can be approximated as

$$\frac{u}{U} = D^2\left(\frac{g^2 \cos\beta}{576\nu^2 Q^2}\right)^{\frac{1}{3}} \ll 1, \tag{2}$$

where D is the bubble diameter according to our above estimates. In our experiments, (2) assumed values on the order of 10^{-3} to 10^{-5}, indicating that the streamline patterns were reasonably close to being accurate.

If the polarity of the electrolysis process is reversed, oxygen, instead of hydrogen, is produced at the wire electrode. In this case, however, the volume of oxygen generated is only half, but the bubbles are much larger than the hydrogen bubbles, resulting in a violation of (2). Hence, the rendered streamline patterns are less accurate.

The bubble-production rate along the electrode is proportional to the electric current. Clutter & Smith (1961) suggest that 1.6 to 3.2 A/m of exposed wire is sufficient. Since the characteristic dimension of a thin liquid film is on the order of 1 mm, the currents required to visualize coating flows are typically < 0.01 A. It follows that a simple 9 V battery is adequate to drive the electrolysis. However, since it is inconvenient to monitor the charge level of the battery and the voltage needed to generate the necessary current depends on the conductivity of the fluid, it is preferable to use a variable d.c. power supply with a range of 0 to 50 V, e.g. Dynascan Corporation, Model 1601.

Fluids with very low conductivity, such as glycerin solutions prepared with distilled water, can be doped with a salt to increase their conductivity and to keep the necessary voltage for the bubble production below 50 V. The electrolysis process in a liquid film, as described above, is accompanied by corrosion, whose strength depends on the type and concentration of the salt added, and the combination of salts and metals present in the flow field. If the inclined plane is made of steel (even stainless steel), it will slowly corrode and dissolve around the wire electrode. This can be costly if not detected early, particularly if the inclined plane is part of a device with a complex geometry. In order to protect against, or at least minimize, corrosion, the following steps are recommended: (i) Consult a corrosion table (Hamner 1974) and look for a fluid–metal–salt combination that exhibits low corrosion activity; and (ii) divert the corrosion activity from the expensive inclined plane to a pair of slave electrodes, built as thin metal shims, located in the outer layers of the sandwich that fastens the bubble wire (see figure 1*a*). This principle is called cathodic protection, and it works only if the slave metal has a lower electrode potential than the metal to be protected. Note that corrosion is not eliminated, but rather focused on the slave material, which can easily be replaced at low cost.

For our system of water–glycerin films on a stainless steel slide, we used 1.27 mm-thick zinc shims as slave electrodes, and sodium bicarbonate ($NaHCO_3$) as salt to increase the fluid conductivity, which resulted in low corrosion activity; hence, there was long and worry-free use of the visualization system. The proper salt

concentration is a function of the liquid viscosity, i.e. the concentration of the glycerin solution; 0.002 g/cm^3 for viscosities of up to $\approx$ 20 mPa s and 0.003 g/cm^3 for up to 70 mPa s were adequate.

Experience has shown that with the main hydrogen-bubble electrode alone, the two *free film surfaces* that are characteristic of premetered coating flows cannot be well visualized. It was necessary to implement additional visualization methods to point out the shapes and positions of these interfaces.

The film surface on the inclined plane that becomes the *coating meniscus* (Ruschak 1985) is optically amplified by a second hydrogen-bubble wire (position B in figure 1*a*), which is pushed through a syringe needle of the appropriate gauge to provide mechanical stability. The needle itself is mounted on a one-dimensional coordinate table coinciding with the plane of the main electrode, allowing the tip of the wire to barely touch the free film surface, whose position is a function of flow parameters. Since the current density at the wire tip is very high, so is the rate of bubble production. Because of the buoyancy effect, the bubbles remain in the film surface and visualize it as a bright, concise line. In figure 1(*a*), the free-surface streamline is also schematically indicated by a dotted line downstream of electrode B.

The second free surface, which displaces air from the substrate to be coated, is called the *wetting meniscus* (Ruschak 1985). It is equivalent to, and formed by, the bottom streamline in the flow field of the liquid film on the inclined plane. This streamline is visualized by a very thin filament of dye, injected through a small hole in the inclined plane. The position of that hole coincided with the bubble plane, and its diameter was 0.508 mm. The flow rate of the dye could be controlled via a micro gear pump (Magnetic Gear Pumps, Series 180–361, Micropump Corporation, Concord, CA), allowing optimum adjustment to varying conditions of the main flow. A water-soluble fluorescent dye was found to be most suitable (Fluorescein Disodium Salt, CAS No. 518-47-8, Eastman Kodak Company). In this manner, the wetting meniscus, including the position of the dynamic wetting line as well as the apparent dynamic contact angle down to microscopic but not molecular dimensions, could be clearly visualized. A dye concentration of 0.003 g/cm^3 of water was sufficient and the compatibility between dye and glycerin permitted matching of the bulk and dye viscosities. Furthermore, the low surface activity of the dye resulted in a static surface-tension difference between bulk and dye solution of $< 2\%$. Finally, the brilliant green hue of the fluorescent material provided an attractive accent on the colour prints. It was visible even on a black-and-white TV monitor.

The hydrogen-bubble tracers are visible only when properly illuminated. Our light source was a 150 W xenon bulb (75 to 200 W Universal Arc Lamp Source, Oriel Corporation, Stamford, CN) whose cylindrical beam was focused and reshaped into a narrow light sheet by a spherical lens and a cylindrical lens in sequence (figure 1*a*). The light sheet concentrated all of the available illumination energy onto the bubble plane to obtain optimum conditions for still photography. In addition, a rotatable mirror allowed us to direct the beam towards any portion of the film flow field.

Optical access into the liquid film from a direction perpendicular to the bubble plane was obtained through a side window (figure 1*b*, *c*). Without this window, the edge of the film wets the slide through a meniscus whose curved surface acts as a lens and strongly distorts the image of the streamline pattern in the bubble plane (figure 2*a*).

The height of the window is critical to the viewing quality. Disturbing edge effects are minimized if its shape exactly matches the film profile. However, coating flows are characterized by highly curved film surfaces whose shapes and positions

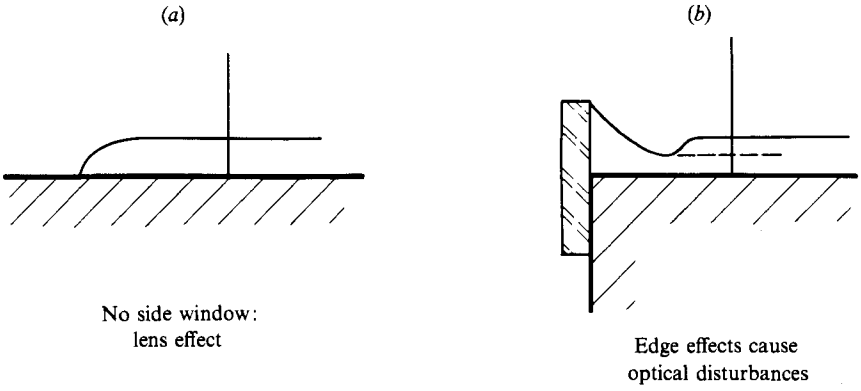

FIGURE 2. Optics and fluid dynamics at the side window.

depend on flow conditions and are unknown *a priori*. Therefore, it is very difficult, if not impossible, to match the side window with the film profile. A typical resulting situation near the film edge is depicted in figure 2(*b*) where the capillary rise of the fluid along the window causes an adjacent depression and the lens effect of the curved film surface may distort or even block the view of the upper part of the streamline pattern. In figure 2(*b*) it is shown how important it is to position the bubble wire far enough away from the window that a truly two-dimensional flow field is observed, and not just some undefined edge effect. We found that a distance of 25 mm was sufficient for a wide range of flow conditions.

We chose a stereo zoom microscope (Stereo Zoom 7, V-1070P with camera adapter, Bausch & Lomb, Rochester, NY) as our magnification device. It offers (i) a working distance of 76 mm, which could be doubled or halved with an auxiliary front lens at the expense of halved or doubled magnification; and (ii) a 7-to-1 variable magnification range, the final magnification of the streamline pattern being dependent on the display medium, e.g. TV monitor, print, or slide. For most typical coating flow fields, a magnification between 20× and 100× is sufficient.

Attached to the microscope was either a black-and-white (Panasonic WV-1850) video camera, which was wired in series to a $\frac{3}{4}$ in. VCR and a black-and-white monitor (see figure 1*b*), or, through a bellows, a 35-mm SLR (Canon A-1) camera body. Film speeds of 400 to 1000 ISO at exposure times of $\frac{1}{4}$ to $\frac{1}{2}$ s rendered good colour, as well as black-and-white, photographs.

As illustrated below, the visualization technique just described is capable of depicting streamline patterns of various small-scale film flows, including coating applications. However, the technique is not without limitations. Besides the necessity for a transparent fluid with good electrolytic properties, and the contamination problem due to dye injection if the liquid is recirculated, there may be optical problems. For example, three-dimensional instabilities and edge effects may lead to film surfaces having a curvature perpendicular to the main flow direction, which might distort, or even eliminate, the view of the streamline pattern.

One major difficulty is related to visualizing a multilayer film whose layers have different physical and optical properties. As can be seen in figure 3, owing to the difference in indices of refraction, n_1 and n_2, the optical path length within the two fluid layers is not equal, and the common streamline pattern of the two-layer film cannot be focused onto the same image plane. Since the depth of focus of microscopes is typically small, it is generally impossible to obtain a sharp image of the entire flow

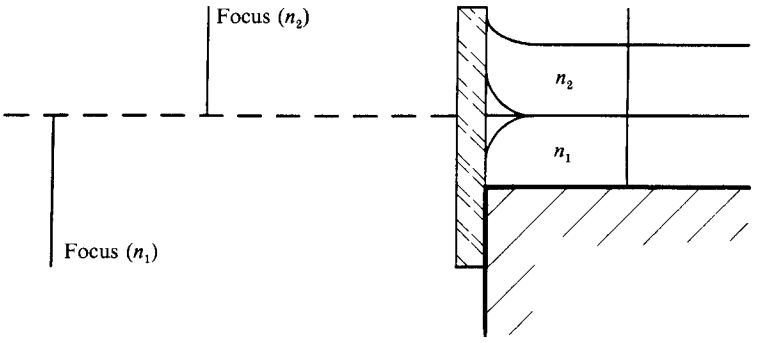

FIGURE 3. Visualization of multilayer films.

field. In addition, the interface between adjacent layers does not necessarily meet the side window at a 90° angle, in which case the interface curvature adds to the optical distortion. These two problems can be eliminated by matching the refractive indices of the fluid layers, taking advantage of the concentration dependence of the refraction index. Adding the proper amount of sodium thiosulfate salt $Na_2S_2O_3 \cdot 5H_2O$, for example, to a water–glycerin solution allows one to adjust n_1 and n_2 while the viscosities and densities of the two layers remain different. However, the procedure is very tedious because the indices have to be matched to at least the third digit after the decimal point; furthermore the viscosity of the second layer can no longer be chosen freely, but becomes a dependent variable owing to the optical matching process. Therefore, in most of our multilayer experiments, we used the same fluid for all layers. Variations of the individual Reynolds numbers were achieved by changing the flow rates.

Another phenomenon of this visualization method refers to optical reflections that appear in all photographs. If the real characteristic dimensions of film flows are considered, the streamline pattern is essentially viewed at the end of a long tunnel or cylinder whose aspect ratio is on the order of 25 to 50. The major boundaries of that cylinder are the surface of the inclined plane, the free and typically curved film surface, and others, e.g. a support to be coated. Since the optical axis of the microscope can, at best, be aligned with only one of these surfaces, the other two act as mirrors in which total reflection of the streamline pattern occurs. The trained eye, however, can easily identify and disregard reflections, inferring the true position and shape of these surfaces from the symmetry lines of the mirror images.

With creativity and imagination, the presented visualization technique can be applied to many different film flow fields. To demonstrate the power of the method, we chose *slide coating*, which is very popular in the photographic industry because it permits premetered multilayer application. Here, a multilayer film is formed first on an inclined plane by means of a hopper, which consists of several elements assembled in a staircase-like fashion (see figure 4). Each element comprises a cavity to distribute the fluid uniformly in the crosswise direction and, when matched with an adjacent element, a narrow slot forms through which the liquid emerges and finally exits as a film onto the inclined plane. At the end of that plane, called the hopper lip, a multilayer film is formed which is subsequently transferred across a narrow gap onto the moving substrate.

It is obvious that such a hopper is most suitable for this visualization technique because the sandwich structure that is used to mount the hydrogen-bubble wire and

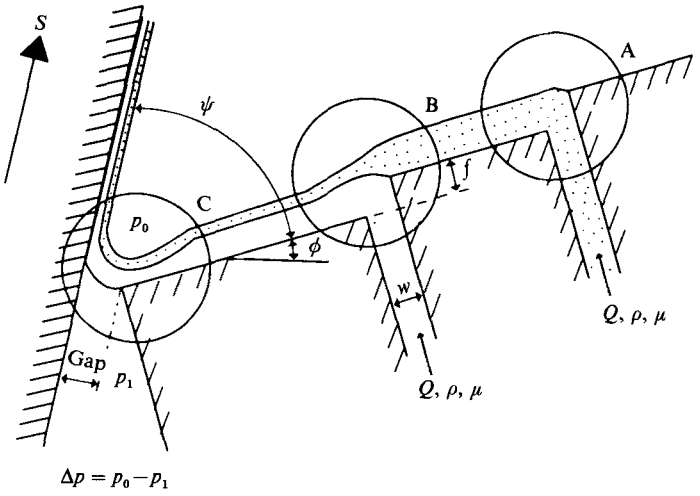

FIGURE 4. Schematic diagram of the slide coating process; forming, merging, and coating of liquid films.

that provides electrical insulation, as well as corrosion protection, can be squeezed between two adjacent elements (see figure 1*a*).

Coating flows are characterized by moderate inertia forces and typical Reynolds numbers cover a range from < 1.0 up to ≈ 100.0. In our experiments, we used water–glycerin solutions of various viscosities. They were supplied from a pressurized tank, filtered, metered by a precision gear pump (Zenith Division, Parker Hannifin Corporation, Waltham, MA), coated onto a polished stainless steel roller 21.6 cm in diameter, then removed by a pressure-loaded rubber squeegee, and colleted in another tank for recirculation. While this situation does not exactly represent the coating process of a photographic emulsion onto a dry substrate, it serves very well to obtain a fundamental understanding of the physics governing small-scale film flows characterized by static and dynamic wetting phenomena.

In the following sections, a selection of characteristic flow fields showing the formation of a liquid film (static wetting, refer to circle A in figure 4), the merging of two fluid layers on an inclined plane (circle B), and the application of a liquid film onto a moving surface (coating or dynamic wetting, circle C) are discussed and illustrated with photographs.

3. The flow field of a forming and merging film

The formation of a liquid film and the merger of two or more layers into a multilayer pack takes place on the hopper slide; and the cross-section of the latter flow field is shown in figure 5 (plate 1). The bottom layer exits from a narrow slot located between adjacent hopper elements, which are slightly offset to form a step in the slide surface. The momentum of the fluid in the slot is low enough that it can turn the 90° corner onto the inclined plane without flow separation. Since there are no tracers in this layer, it appears black on the photograph. The top layer is formed likewise, two hopper elements upstream of this slot. However, the fluid is now moving past two hydrogen-bubble wires, one of which is sandwiched between hopper elements and extends through the flow field. The other one just touches the free film surface, which shows up as a bright white line. Note that the faint white lines above

the film surface and also in the hopper elements are reflections and can be disregarded.

This flow field represents near-optimum conditions. The streamlines describe an almost rectilinear pattern, indicating no convective mixing between adjacent fluid layers, which is essential in manufacturing photographic products. Moreover, the step height has been adjusted to the flow parameters of the bottom layer, particularly its film thickness, so that the fluid–fluid interface, which originates at the corner of the upstream hopper element, does not excessively disturb either layer. Finally, the film surface in the merging area is flat, not revealing any details of the flow field beneath.

However, if the flow rate or the momentum of the bottom layer is increased above a critical value, the fluid is not able to turn around the sharp corner without separating from the slide surface; the result is a vortex tube that extends all across the film (figure 6, plate 1). Since there are no tracers in the bottom-layer fluid, this vortex was made visible by releasing bubbles from the tip of a third wire, which was temporarily lowered into the separated liquid.

In strictly two-dimensional flows, the main stream is divided from the vortex by the separating streamline, which connects the rear and forward stagnation points located on the flow boundary. Then, by definition, no fluid can cross that streamline. Through dye injection into the vortex tube, we observed that the flow there is not two-dimensional, as was first assumed, but rather, three-dimensional. The fluid is shown spiralling along the vortex axis from the centre of the tube towards both sidewalls, which confine the film to the slide. In the vicinity of the depression in the film profile (see figure 2*b*), the vortex turns around a 90° corner and, like a horseshoe, is convected downstream in the direction of the main flow. The helical crossflow in the separation bubble leads to a drainage of that fluid; consequently, new liquid from the main flow must cross the separation streamline in order to feed and maintain the size of the vortex. This phenomenon is a classic end effect due to an adjustment of the shear and pressure forces acting on the recirculating fluid to the no-slip boundary condition imposed by the sidewalls. Similar situations have been observed in other types of flow fields, for example, in the driven cavity flow (Koseff & Street 1984). These authors report that the outflow from the vortex becomes stronger with increasing Reynolds number. Moreover, the size of the vortex depends on the width of the flow field, and the cross-section is not uniform, but smaller towards the sidewalls than in the centre. These observations could be confirmed for the vortex shown in figure 6. In addition, we noticed that it became larger as the Reynolds number was increased.

These facts explain why vortices are not desirable in coating flows. Their presence not only broadens the residence-time spectrum of the system, but the throughflow of liquid in the vortex allows particles and bubbles to get trapped, at least temporarily, which may cause the uniformity of the coated product to decrease.

If the flow rate of the bottom layer is increased still further, so is the jetting effect, and the vortex downstream of the corner increases in size. In addition, the liquid–liquid interface penetrates deeply into the top layer, forcing the flow field to become highly two-dimensional. If the Reynolds number of the top film is low enough, a second vortex attached to the free surface may form (see figure 7, plate 2). As will be shown, the flow field strongly resembles that of a liquid layer being coated onto a dry moving substrate. In fact, the merging of two fluid films as presented here is nothing but a coating process where one layer is being coated onto another.

Coating or dynamic wetting processes are characterized by a Sakiadis-type

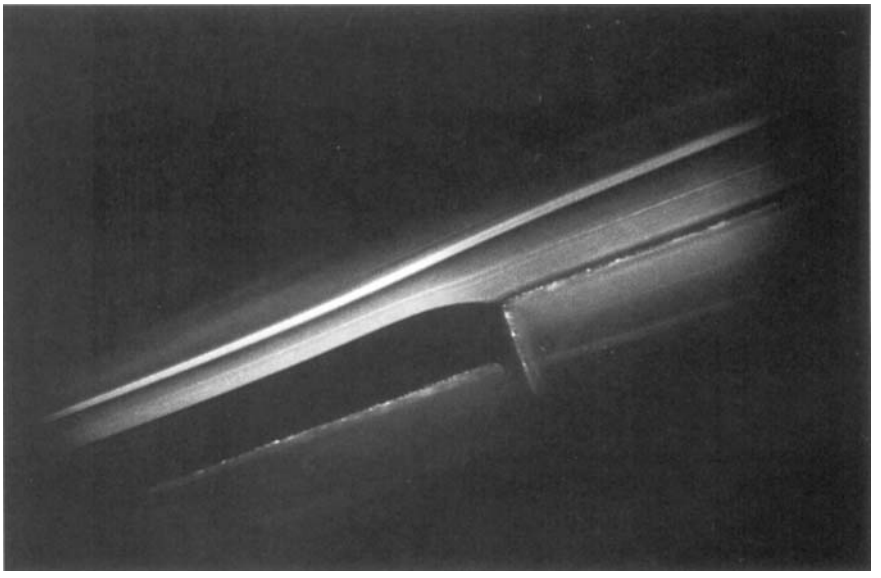

FIGURE 5. Merging of two liquid layers on an inclined plane; near optimum flow field. *Re* (bottom) = 11.6; *Re* (top) = 12.9, *Po* = 1.7 × 10^{-6}; ϕ = 15°; w = 254 μm; f = 508 μm.

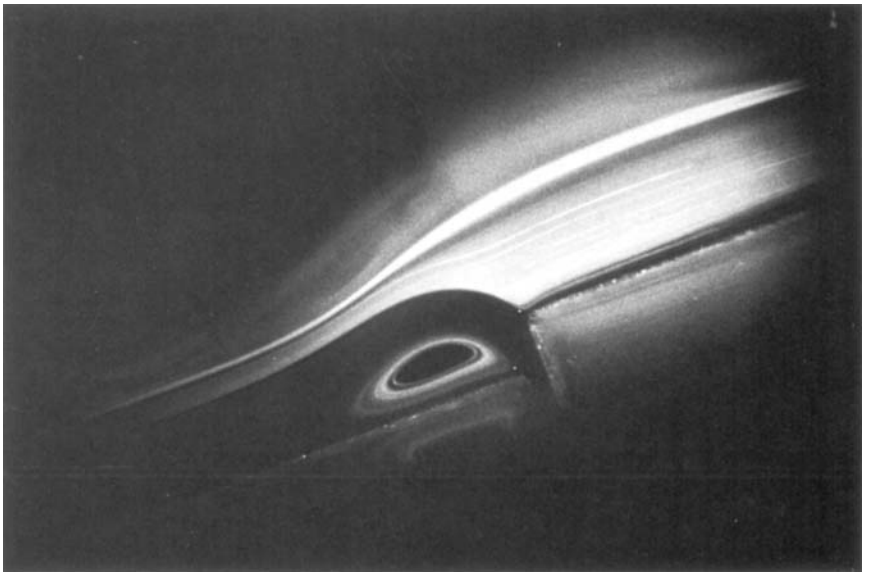

FIGURE 6. Merging of two liquid layers on an inclined plane; single vortex. *Re* (bottom) = 24.8; *Re* (top) = 12.8, *Po* = 1.7 × 10^{-6}; ϕ = 15°; w = 254 μm; f = 508 μm.

(Facing p. 294*)*

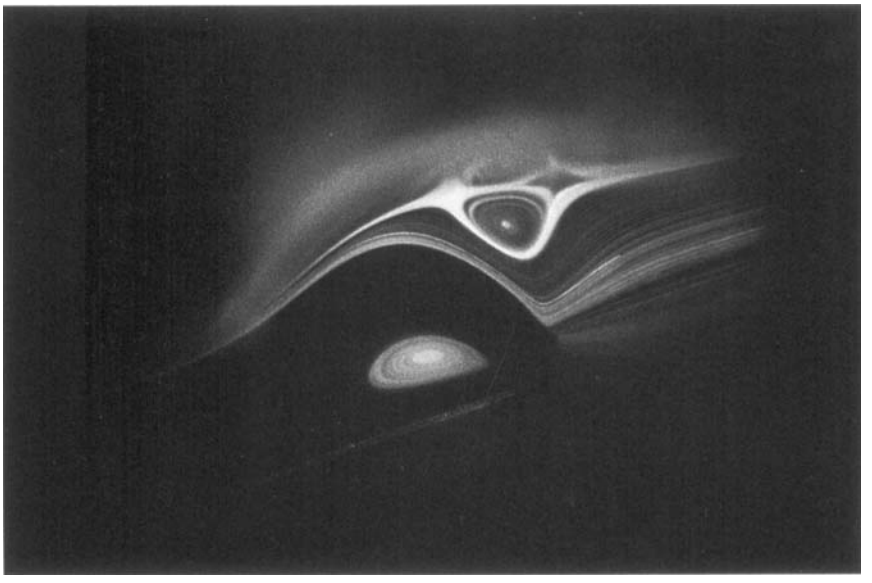

FIGURE 7. Merging of two liquid layers on an inclined plane; multiple vortices. *Re* (bottom) = 15.5; *Re* (top) = 3.0; $Po = 2.5 \times 10^{-6}$; $\phi = 15°$; $w = 254$ μm; $f = 508$ μm.

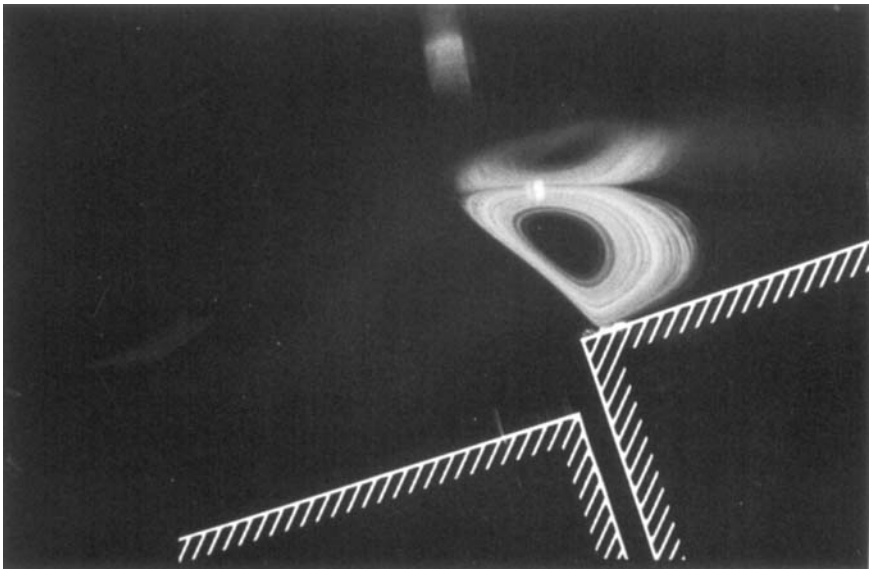

FIGURE 8. Formation of a free film surface; migration of the static wetting line upstream of the sharp corner. $Re = 18.3$, $Po = 3.0 \times 10^{-6}$; $\phi = 15°$; $w = 508$ μm; $f = 940$ μm.

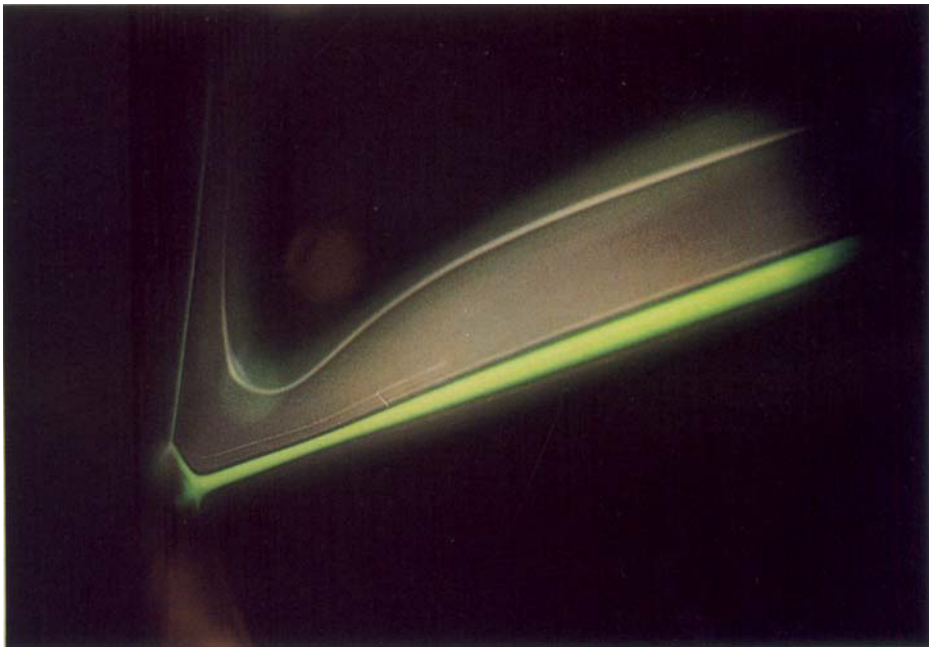

FIGURE 10. Single-layer coating; near optimum flow field. $Re = 6.4$; $Ca = 0.320$; $Po = 4.7 \times 10^{-5}$; Gap = 483 μm, $\Delta p = 75.0$ Pa; $\psi = 50°$; $\phi = 15°$.

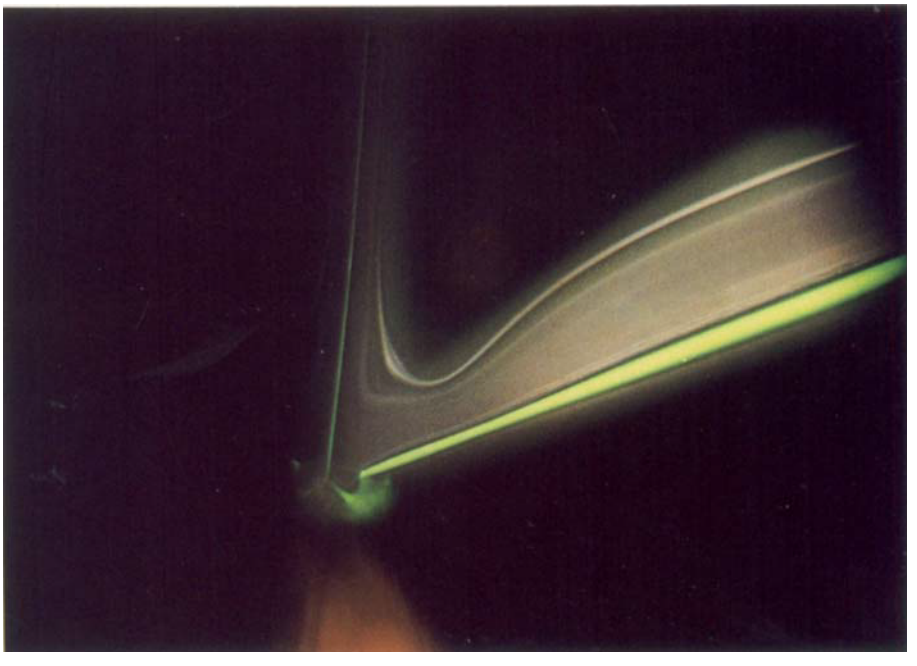

FIGURE 11. Single-layer coating; the effect of the pressure difference across the liquid bridge. $Re = 6.4$; $Ca = 0.320$; $Po = 4.7 \times 10^{-5}$; Gap = 483 μm; $\Delta p = 299.0$ Pa; $\psi = 50°$; $\phi = 15°$.

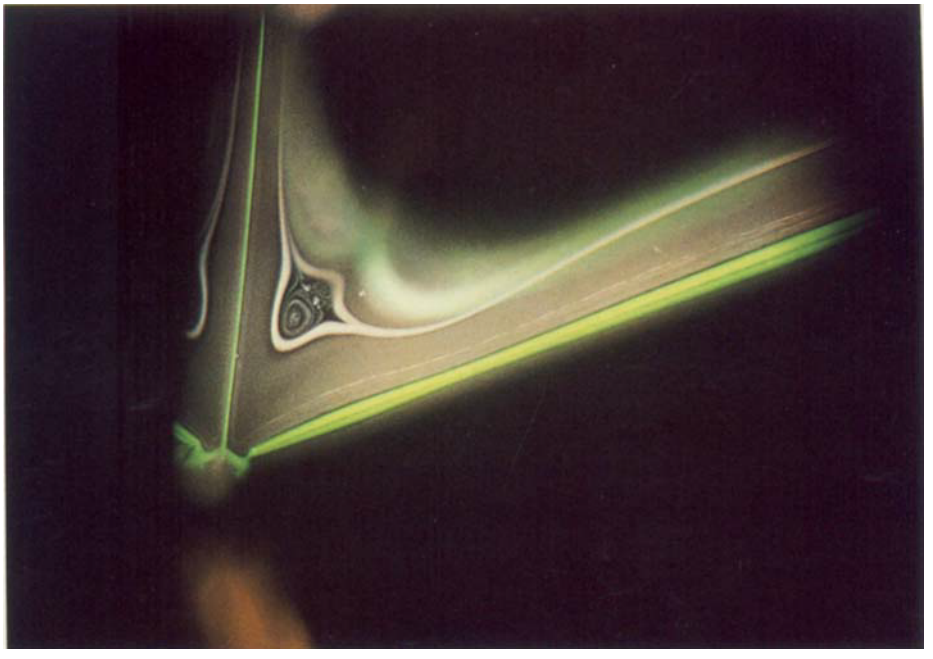

FIGURE 12. Single-layer coating; flow separation (vortex #1). Re = 3.2; Ca = 0.120; Po = 4.7 × 10^{-5}; Gap = 483 μm, Δp = 75.0 Pa; ψ = 50°; ϕ = 15°.

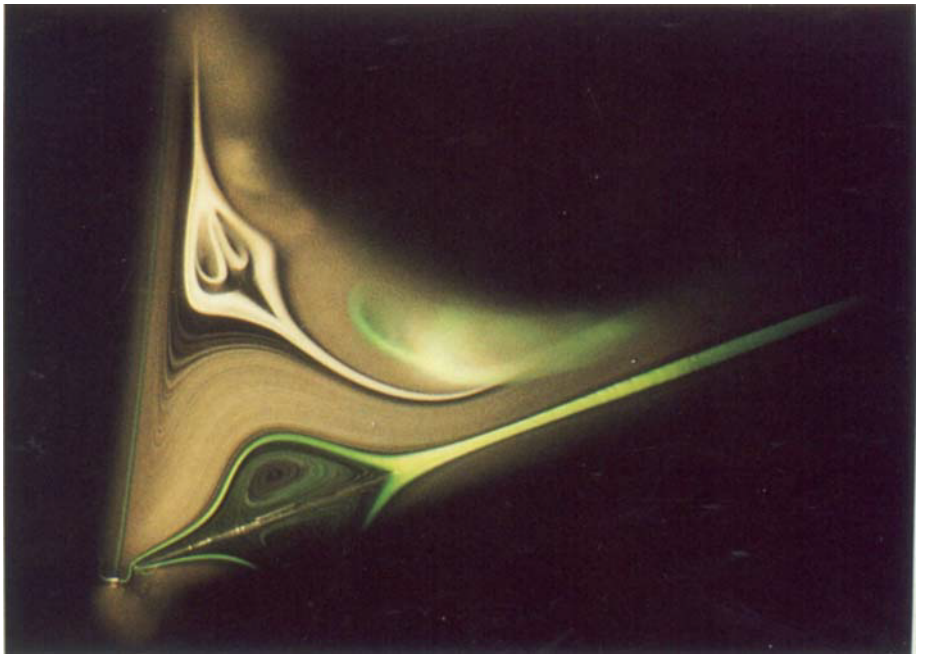

FIGURE 13. Single-layer coating; multiple vortices. Re = 31.0; Ca = 0.077; Po = 8.1 × 10^{-8}; Gap = 254 μm, Δp = 0 Pa; ψ = 50°; ϕ = 15°.

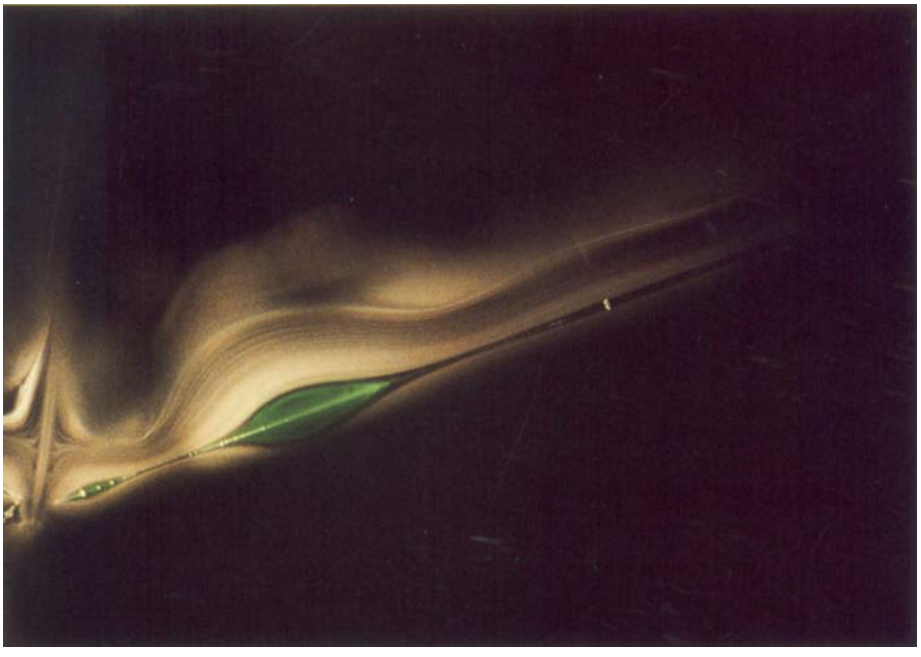

FIGURE 14. Single-layer coating; standing waves and multiple vortices. Re = 88.7; Ca = 0.069; Po = 2.9 × 10^{-9}; Gap = 254 μm; Δp = 0 Pa; ψ = 50°; ϕ = 15°.

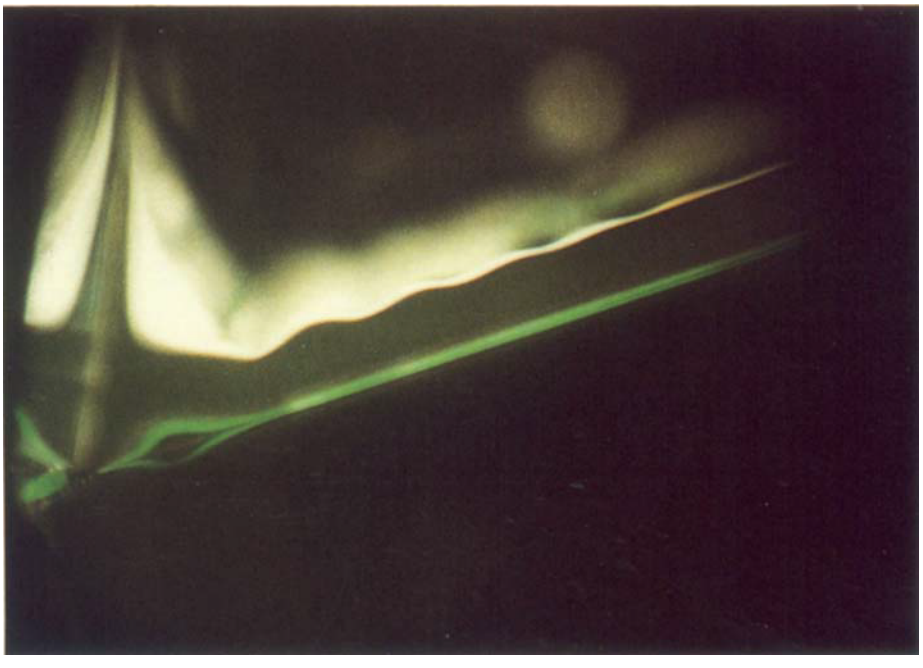

FIGURE 15. Single-layer coating; standing waves. Re = 162.6; Ca = 0.196; Po = 2.9 × 10^{-9}; Gap = 254 μm; Δp = 0 Pa; ψ = 50°; ϕ = 15°.

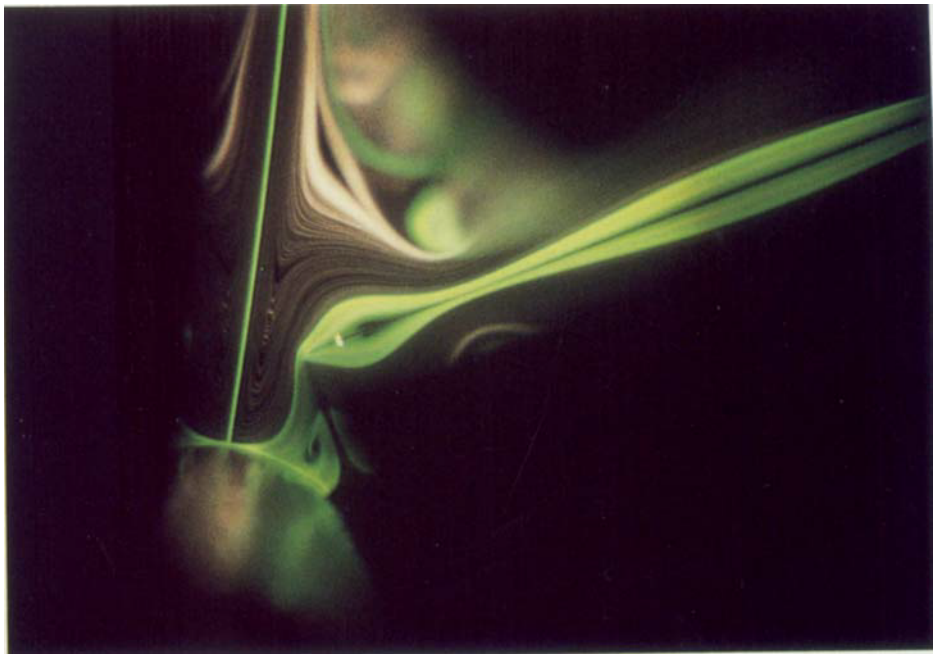

FIGURE 16. Single-layer coating; flow around the tip of the hopper slide. Re = 36.1; Ca = 0.075; $Po = 4.5 \times 10^{-8}$; Gap = 762 μm, Δp = 0 Pa; $\psi = 50°$; $\phi = 15°$.

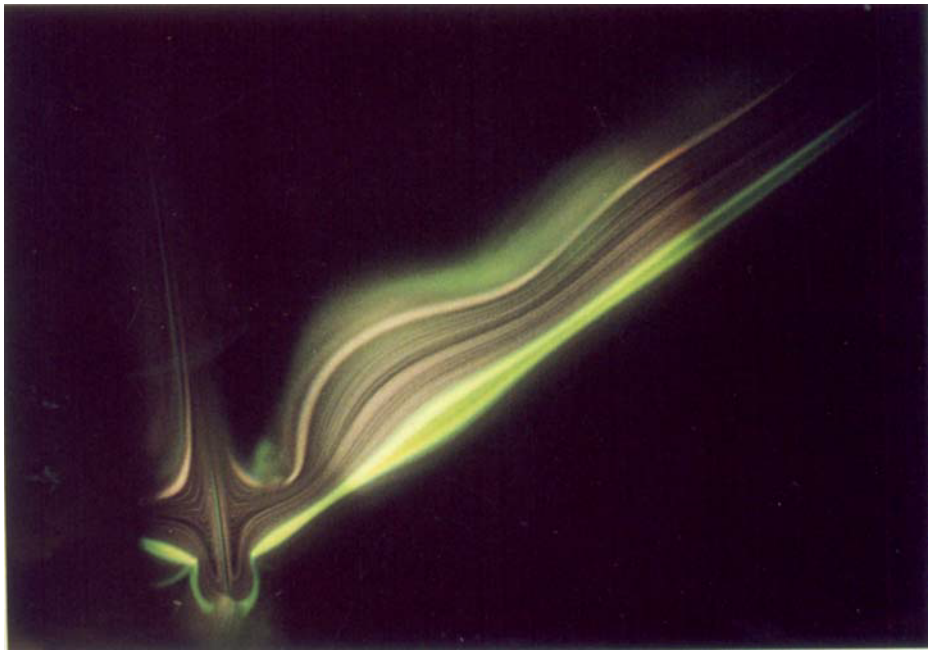

FIGURE 18. Single-layer coating; comparison between experimental and theoretical flow-visualization techniques. Re = 45.0; Ca = 0.208; $Po = 4.5 \times 10^{-8}$; Gap = 330 μm; Δp = 162.0 Pa; $\psi = 60°$; $\phi = 30°$.

boundary layer (Sakiadis 1961) which originates at the dynamic wetting line, or at the point where the fluid to be coated first strikes the moving substrate. In figure 7, this point coincides with the downstream corner of the upstream hopper element. Only fluid located inside the boundary layer is able to experience the viscous drag force and the acceleration effect of the moving substrate. If the fluid supplied by the top layer is entrained into the boundary layer before its length reaches the free film surface, whose shape and position is determined by local pressure and capillary forces as well as geometric parameters, then a void area will result, which is filled with circulating liquid. As shown in figure 7, the separation bubble attaches to the free film surface.

4. The flow field near a static wetting line

One of the two free surfaces that are pertinent to premetered coating flows is generated at the uppermost slot on the hopper slide (see figure 4, circle A). The flow field near the downstream corner of the top element is characterized by a static wetting line and its details are determined by capillary-hydrodynamic and geometric parameters.

For low step heights and clean hopper surfaces, we have observed experimentally that it is possible for the static wetting line to be pinned at the corner. If the flow rate is high, then the jetting effect will lead to a highly curved, convex film surface above the slot exit (see also Kistler 1983, chapter 4); these conditions are unstable. Small disturbances, ever present in laboratory environment, will cause the wetting line to move upstream along the surface of the top element to some unknown position. The result is a wedge of liquid, separated from the main flow by a steamline connecting the element corner with a stagnation point located on the free surface above the corner, and filled with a series of vortices whose size and strength decrease in the upstream direction. In figure 8 (plate 2), the steamline pattern of the first and strongest wedge vortex is visualized by hydrogen bubbles.

Conversely, for large step heights and low flow rates, the static wetting line is located on the element surface downstream of the corner, and its position is governed by the capillary rise of the liquid along that surface. In the case of high wettability, the small contact angle will again result in a wedge of fluid. Since the main flow is not able to penetrate all the way to the vertex of the wedge, it too is filled with a series of vortices. Such wedge or corner vortices were analysed theoretically by Moffatt (1964), and an excellent photograph of multiple vortices in a driven wedge-shaped cavity was produced by Taneda (1979) and published in Van Dyke's *Album of Fluid Motion* (1982).

If the static wetting line is not pinned to the sharp corner, it will most likely, owing to surface roughness and contamination, describe an irregular path across the film, which may result in decreased uniformity of the coated product. It is, therefore, important to know under what conditions the wetting line will adhere to the corner. The issue is rather complicated; most theoretical arguments presented in the literature are based on thermodynamic or mechanical considerations (Blake 1984). The starting point is Young's equation (Young 1805), which provides a necessary condition for the hydrostatic equilibrium of a wetting line located on a flat surface. Gibbs (1906) expanded this condition to the case where the wetting line is pinned at a sharp corner. An experimental verification thereof, at least for corners having a sharpness approaching molecular dimensions, was provided by Oliver, Huh & Mason (1977). Finally Kistler (1983) has shown that the Gibbs condition is valid even for

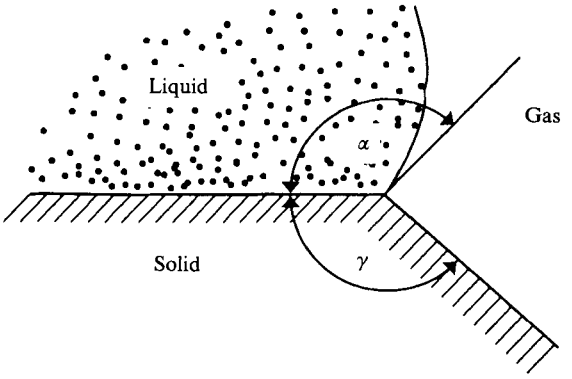

FIGURE 9. The inhibiting effect of a sharp corner on the migration of a static wetting line.

dynamic situations, i.e. in the presence of flow near the wetting line, and he presents the inhibiting effect of a sharp corner on the migration of a wetting line in the following way (see figure 9):

Contact-line advance and retreat are inhibited, as long as

$$\alpha \leqslant 180^\circ - \gamma + \theta_A \tag{3a}$$

and

$$\alpha \geqslant \theta_R, \tag{3b}$$

respectively. Here, α is the separation angle of the fluid interface from the solid surface, γ is the corner angle, and θ_A and θ_R are the advancing and receding contact angles, respectively. Owing to static and dynamic contact-angle hysteresis effects, Gibbs' inequality conditions (3*a*, *b*) are necessary, but not sufficient; they set upper and lower bounds on the separation angle α for the wetting line to be pinned at the corner.

In many industrial environments, the contact angles θ_A and θ_R are relatively small, indicating good wetting of the solid by the fluid, but, typically, exact values are not known owing to contaminated surfaces. Moreover, the separation angle α is generally not known either, and it may vary over a considerable range, depending on flow conditions. Given this situation, inequality condition (3) indicates that the range for the separation angle α, which permits configurations with pinned contact lines, can be maximized by minimizing the corner angle γ. In practice, however, safety considerations on sharp corners and arguments on mechanical stability and rigidity set lower limits for γ.

5. The flow field of a coating process

At the end of the inclined plane, the liquid film detaches itself from the hopper lip, bridges a narrow gap on the order of 100 μm, and is applied onto the moving substrate. This process is shown in figure 10 (plate 3) for near-optimum conditions. As can be seen, the free surface of the liquid film just upsteam of the coating point is characterized by a concave meniscus of high curvature, owing to the sharp change in flow direction. The capillary pressure drop across that meniscus leads to a subatmospheric liquid pressure, and the accompanying acceleration causes the film to thin.

The bottom streamline of the film on the slide is indicated by a fluorescent dye

filament. Note that, because of reflections in the hopper slide, the filament appears twice as thick as it is in reality. At the end of the inclined plane, the bottom streamline leaves the hopper lip at the static wetting line, which for these conditions is pinned to the sharp corner. It is at this point that the second of the two characteristic free surfaces of premetered coating flows is formed, and the forces governing the local flow field are very similar to those in the situation near the static wetting line upstream at the top of the hopper slide (figure 8). As indicated by the thinning of the green dyeline, the liquid must accelerate from zero velocity at the static contact line to web velocity at the dynamic wetting line where the fluid first strikes the support. The curvature of the second free surface, which is often called the lower meniscus, depends on the local pressure and stress field in the liquid film, on the position of the dynamic wetting line, and on the pressure in the chamber below the liquid bridge, which is, typically, held several millimetres of water below atmospheric. The meniscus can be straight, as in figure 10, but convex or concave shapes are also possible.

At the dynamic wetting line, a boundary layer of the Sakiadis type begins, much like the one described in figure 7. Only the liquid entrained into the boundary layer is able to experience the viscous drag force of the moving support. The thickness of the boundary layer grows in the downstream direction until all the fluid flowing down the inclined plane has been entrained. That liquid is being accelerated, and at the point where all fluid elements travel at web speed, the film on the support will have reached its final wet thickness.

The flow field in figure 10 is near optimum because it is free of vortices; the streamlines describe a smooth, though complex, pattern without crossing each other, which is essential in photographic multilayer coating, and the apparent dynamic contact angle, i.e. the angle between the support and the lower meniscus as measured across the fluid, is $< 180°$, indicating conditions remote from air entrainment (Blake & Ruschak 1979; Gutoff & Kendrick 1982; Kistler, Hanauska & Scriven, 1984).

In slide coating, the pressure in the chamber below the liquid bridge is often used to control the performance of the coating process. The effect of that parameter on the local flow field is shown in figure 11 (plate 3), where all conditions are identical with those in figure 10, except that the pressure has been lowered to 299 Pa (30.5 mm of water) below ambient. The primary result is the migration of the dynamic contact line upstream along the moving web. This, in turn, enlarges the separation angle α at the static wetting line so that the Gibbs inequality condition ($3a$) is violated; consequently, the static contact line migrates to a new equilibrium position below the sharp corner of the hopper lip. Although it is not clearly visible in figure 11, the flow field there must look similar to the one shown in figure 8, with a relatively small advancing contact angle and a series of vortices characteristic of a separated wedge of fluid driven by an outer flow.

It will be further discussed below that if, for a given capillary number Ca, the Reynolds number Re is below a critical value, then the point on the boundary layer at which all the fluid flowing down the inclined plane has been entrained into the boundary layer is located not on the upper meniscus, but somewhere inside the flow field. In such cases, the streamline of the free film surface must branch away from it at a stagnation point in order to meet that distinct point on the boundary layer, and farther downstream, to rejoin the upper meniscus at a second stagnation point. In figure 12 (plate 4), the resulting void area in the flow field is filled with an eddy whose fluid is circulating in the clockwise direction. Note that part of the eddy streamline

pattern is reflected and the true position of the free liquid surface is given by the symmetry line of the mirror image. In addition, note the similarities in character between the vortex in figure 12 and the eddy attached to the film surface in figure 7.

Premetered coating flows are a combination of a stagnation-point flow and a viscous boundary-layer flow. The degree to which each of these flow types is developed depends on the operating conditions, the physical properties of the fluid, and the geometric parameters (figure 13, plate 4). The liquid stream flowing down the inclined plane is impinging on the moving substrate, which is oriented somewhat perpendicular to the main flow direction, and the streamline pattern clearly indicates the dividing effect of the stagnation-point flow. In fact, fluid elements that are only a fraction of a millimetre away from the substrate are still moving opposite to the web direction. Only after these fluid elements have penetrated the boundary layer (whose location is nicely visualized by the sharp bends in the streamlines) do they experience the viscous drag of the substrate, at which point they are accelerated and convected downstream.

As shown in figure 13, the pressure increase in the flow direction characteristic of stagnation-point flows may result in a second separation bubble, attached to the inclined plane itself and located just upstream of the hopper lip. All these vortices in the flow field near the coating point are also plagued by edge effects. The separated fluid spirals in a three-dimensional fashion and corner eddies are present where the liquid film is terminated by side rails.

At high Re and Ca, the slight thickening and subsequent thinning of the liquid film at the end of the hopper slide (figure 10) become much more pronounced. In fact, a second, but smaller, wave forms upstream on the slide. This pattern is called *standing waves*, as shown in figure 14 (plate 5). Standing waves are observed where a liquid film or jet flows into a large pool, or against an obstacle put in the main flow direction, such as the moving substrate at the end of the inclined plane. The mechanism for this phenomenon was described by Ruschak (1978). The wavy film surface is the result of an interaction between viscous stress gradients and capillary pressure gradients such that the film profile far upstream blends smoothly with the highly curved upper meniscus of the liquid bridge.

Note that the positive pressure gradient beneath each wave crest generates conditions favourable to flow separation, and slide coating flow fields with multiple vortices on the hopper slide are possible (see figure 14).

Increasing Re still further while keeping Ca high amplifies the series of standing waves whose amplitudes decrease quickly in the upstream direction (figure 15, plate 5). The lowermost wave and the film thinning due to the meniscus curvature are less pronounced here than for the conditions in figure 14, but multiple vortices as shown in figure 13 are still possible. The out-of-focus streamline pattern in figure 15 is due to the high substrate speed of 4.23 m/s, which resulted in vibrations in the entire experimental set-up.

On the other hand, if the web speed is very low and the gap between the hopper lip and the substrate is large, then the stagnation-point flow character is quite distinct, resulting in a dynamic wetting line located far upstream on the substrate and below the tip of the inclined plane, as shown in figure 16 (plate 6). For these conditions, the separation angle α at the static wetting line could not satisfy Gibbs' inequality condition ($3a$) if the film were detached from the tip of the hopper lip. Instead, the equilibrium position for the static contact line is far downstream on the hopper element, resulting in a very small advancing contact angle θ_A. For certain operating conditions, there may even be complete wetting (a condition known as

'pull through'), meaning that not all the fluid supplied down the slide is being coated onto the web. As in figure 8, the flowing film is not able to penetrate the shallow wedge of fluid, but it provides the driving force for the rotation of the series of vortices there, the first of which is visualized by streams of fluorescent dye.

If the web speed in figure 16 were just slightly lower, the dynamic wetting line could move still deeper into the gap and a stagnation point would form in the centre of the flow field below the tip of the hopper slide. It turns out that such a situation leads to an oscillatory instability, owing to the presence of a non-orthogonal saddle point (O'Brien 1981) located above that stagnation point. High shear forces are generated there by streamlines circling around the centre stagnation point and by streamlines from the upper portion of the film on the slide, which approach the saddle point from the opposite direction.

6. Comparison between theoretical and experimental flow visualization

Christodoulou & Scriven (1984) presented a parameter study of slide coating generated by the finite-element method. They showed streamline plots that revealed details of the inside of the flow field, including areas of flow separation. One example is depicted in figure 17(*a*). They assumed that the static wetting line was pinned at the tip of the hopper lip; they also assumed a value for the apparent dynamic contact angle, as well as some local slip, near the dynamic contact line. The resulting flow field is characterized by standing waves and two vortices on the inclined plane.

We decided to duplicate these conditions in our laboratory for experimental verification of the theoretical predictions, and the streamline pattern is shown in figure 18 (plate 6). It can be seen that the static wetting line is not pinned at the sharp corner, but is located somewhere below the hopper lip. This allows the fluid to flow around the corner, and the 'real' flow field near the coating point is quite different from the one predicted by the finite-element method. In particular, note that there are no areas of flow separation on the inclined plane. We then measured the apparent static and dynamic contact angles from our photograph and passed the values on to Christodoulou. He generated a revised streamline plot (figure 17*b*), with our experimentally determined contact angles and the previously assumed slip coefficient, which has been shown to affect the local flow field only slightly near the wetting line (Kobayashi *et al.* 1982).

Now, the agreement between the theoretical and experimental flow field along the lower meniscus is remarkable. The small remaining differences regarding the film profile of the upper meniscus cannot be explained at present. They may be due to an inappropriate finite-element grid or dynamic surface-tension effects, since our test fluid contained traces of fluorescent dye.

So it appears that the finite-element method is capable of calculating complex free-surface flow fields such as slide coating, but the lack of knowledge of the boundary conditions at the static and dynamic contact lines is a severe drawback. It is clear that the most successful approach is a combination of theoretical and experimental flow-visualization methods.

7. The onset of flow separation

Although the flow field of slide coating is characterized by numerous potential sites for flow separation, these vortices are present for a given apparatus geometry only if certain flow parameters exceed a critical value called the inception point. For such

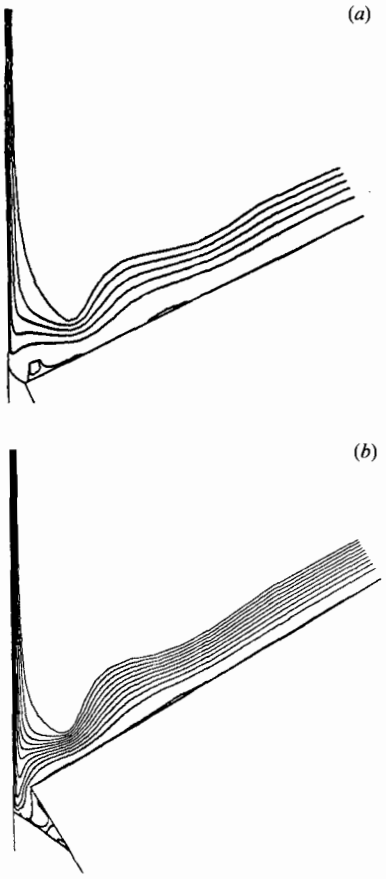

FIGURE 17. Finite-element simulation of the slide coating process by Christodoulou & Scriven (1984). (*a*) The boundary conditions at the static and dynamic wetting lines were unknown and had to be assumed. (*b*) The boundary conditions at the static and dynamic wetting lines were determined from figure 18. $Re = 45.0$; $Ca = 0.208$; $Po = 4.5 \times 10^{-8}$; Gap = 330 μm; $\Delta p = 162.0$ Pa; $\psi = 60°$; $\phi = 30°$.

conditions, the eddies are infinitesimally small; but, if those flow parameters continue to change, the size of the vortices and the strength of the fluid rotation increase. This process seems reversible without appreciable hysteresis. The visualization method is well suited to experimentally determine the onset of vortices in coating flows.

Figure 19 shows an example of such data for the eddy in figure 12, which is located on the upper meniscus and arbitrarily named vortex No. 1. The geometry of the apparatus is defined by a slide ϕ of 15° and an angle ψ between the hopper slide and the tangent to the coating roll of 50°. $Ca = \mu S/\sigma$ is plotted versus $Re = \rho Q/\mu$ for different values of the property number, $Po = g\mu^4/\rho\sigma^3$. Here, ρ is the density, μ is the dynamic viscosity, σ is the surface tension, g is the gravitational acceleration, Q is the volumetric flow rate per unit width, and S the speed of the substrate. Vortex No. 1 is present in the flow field for a fixed Re if Ca is less than the critical value given by the corresponding curve.

The symbols in figure 19 are experimental data points, whereas the solid lines resulted from a nonlinear regression on those data. This analysis showed no statistically significant dependence of the onset of vortex No. 1 on the pressure

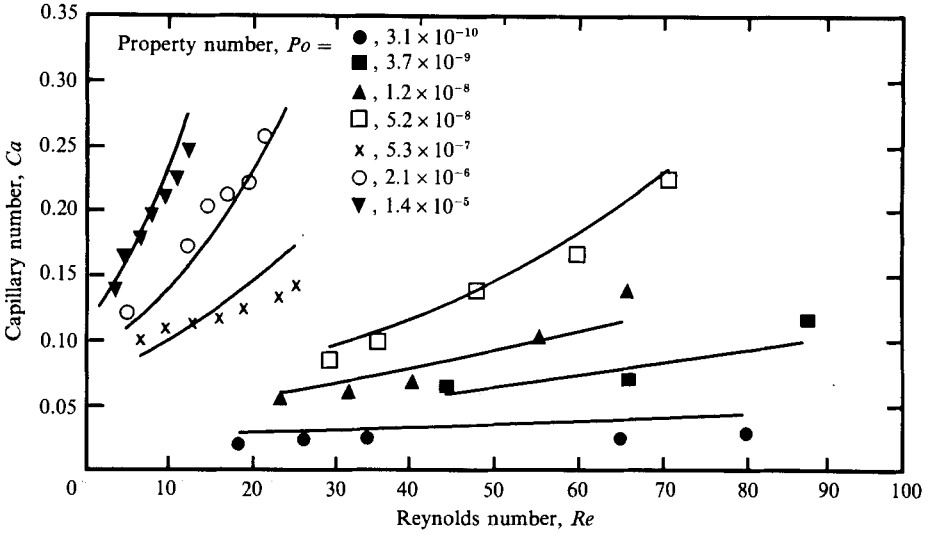

FIGURE 19. The onset of flow separation (vortex No. 1).

difference across the liquid bridge nor on the gap between hopper lip and substrate. An analytical expression of the onset criterion for vortex No. 1 was constructed by graphically displaying and analysing the experimental data. Its form is given by

$$Ca = A\,Po^{B} \exp\left[C\,Re\,Po^{D}\right]. \tag{4}$$

The regression parameters are $A = 0.5406$, $B = 0.1441$, $C = 0.8434$, and $D = 0.2170$. The quality of the fit is expressed by an r^2-value of 0.942.

8. Summary

Despite their small characteristic dimensions, premetered coating flows can be successfully visualized by careful experimentation. The method presented here produces good photographs of streamline patterns, revealing clear information on the shape and position of free liquid surfaces, including standing waves and apparent dynamic contact angles. Moreover, visualization of distinct features, such as stagnation point and boundary-layer flow characteristics, as well as flow separation and flow fields near static wetting lines, is possible. In addition, our experimental technique is compared with theoretical flow visualization performed on a computer using the finite-element method, and we present a sample data set for the onset of vortices.

We hope that our photographs will stimulate new research efforts in the areas of coating and dynamic wetting. We also hope that they demonstrate that coating flows have artistic and aesthetic character, in addition to their technical nature.

This work was carried out during my employment at the Manufacturing Technology Research Laboratories, Eastman Kodak Company, Rochester, New York 14650. I am grateful for the opportunity to publish the results.

REFERENCES

BLAKE, T. D. 1984 Wetting. In *Surfactants* (ed. Th. F. Tadros), Chap. 10, Academic.

BLAKE, T. D. & RUSCHAK, K. J. 1979 *Nature* **282**, 489–491.

BURLEY, R. & KENNEDY, B. S. 1976 *Br. Polym. J.* **8**, 140–143.

CLUTTER, D. W. & SMITH, A. M. O. 1961 *Aerospace Engng* **1**, 24–76.

CHRISTODOULOU, K. N. & SCRIVEN, L. E. 1984 *AIChE Annual Meeting, San Francisco, CA, Paper* 1423.

GIBBS, J. W. 1906 *The scientific papers of J. W. Gibbs. Vol. I, Thermodynamics*, pp. 314–331. Longmans, Green.

GUTOFF, E. B. & KENDRICK, C. E. 1982 *AIChE J.* **28**, 459–466.

HAMNER, N. E. 1974 *Corrosion data survey*. National Assoc. of Corrosion Engineers, Houston, TX.

KISTLER, S. F. 1983 The fluid mechanics of curtain coating and related viscous free surface flows with contact lines. Thesis, University of Minnesota, Minneapolis.

KISTLER, S. F., HANAUSKA, C. P. & SCRIVEN, L. E. 1984 *AIChE WinterMeeting, Atlanta, Georgia, Paper* 17a.

KISTLER, S. F. & SCRIVEN, L. E. 1983 Coating flows. In *Computational Analysis of Polymers* (ed. J. Pearson & S. Richardson), Chap. 8. Barking.

KOBAYASHI, C., SAITO, H. & SCRIVEN, L. E. 1982 *AIChE Winter Meeting, Orlando, Florida, Paper* 45e.

KOSEFF, J. R. & STREET, R. L. 1984 *Trans. ASME: J. Fluids Engng* **106**, 385–389.

KRAEGEL, J., FRUHNER, H. & KRETZSCHMAR, G. 1987 *J. Inf. Rec. Mater.* **15**, 251–257

MOFFATT, H. K. 1964 *J. Fluid Mech.* **18**, 1–18.

OLIVER, J. F., HUH, C. & MASON, S. G. 1977 *J. Colloid Interface Sci.* **59**, 568–581.

O'BRIEN, V. 1981 *Phys. Fluids* **24**, 1005–1009.

RUSCHAK, K. J. 1978 *AIChE J.* **24**, 705–709.

RUSCHAK, K. J. 1985 *Ann. Rev. Fluid Mech.* **17**, 65–89.

SAKIADIS, B. C. 1961 *AIChE J.* **7**, 221–225.

SCHRAUB, F. A., KLINE, S. J., HENRY, J., RUNSTADLER, JR, P. W. & Littell, A. 1965 *Trans. ASME: J. Basic Engng* **87**, 429–444.

SCHWEIZER, P. M. & SCRIVEN, L. E. 1983 *Phys. Fluids* **26**, 619–623.

TALLMADGE, J. A., WEINBERGER, C. B. & FAUST, H. L. 1979 *AIChE J.* **25**, 1065–1072.

TANEDA, S. 1979 *J. Phys. Soc. Japan* **46**, 1935–1942.

VAN DYKE, M. 1982 *An Album of Fluid Motion*. Parabolic.

YOUNG, T. 1805 *Phil. Trans. R. Soc. Lond.* **95**, 65.